

A feasibility study of X-ray phase-contrast mammographic tomography at the Imaging and Medical beamline of the Australian Synchrotron

Yakov I. Nesterets,^{a,b*} Timur E. Gureyev,^{a,b,c,d} Sheridan C. Mayo,^a
Andrew W. Stevenson,^{a,e} Darren Thompson,^{a,b} Jeremy M. C. Brown,^d
Marcus J. Kitchen,^d Konstantin M. Pavlov,^{b,d} Darren Lockie,^f
Francesco Brun^{g,h} and Giuliana Tromba^h

Received 26 May 2015

Accepted 21 September 2015

Edited by A. Momose, Tohoku University, Japan

Keywords: X-rays; phase contrast; computed tomography; mammography.

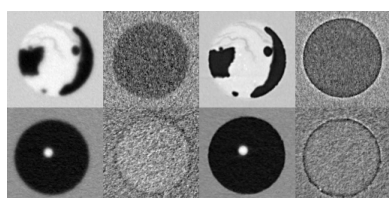
^aCommonwealth Scientific and Industrial Research Organisation, Melbourne, Australia, ^bSchool of Science and Technology, University of New England, Armidale, Australia, ^cARC Centre of Excellence in Advanced Molecular Imaging, School of Physics, The University of Melbourne, Parkville, Australia, ^dSchool of Physics and Astronomy, Monash University, Melbourne, Australia, ^eAustralian Synchrotron, Melbourne, Australia, ^fMaroondah BreastScreen, Melbourne, Australia, ^gDepartment of Engineering and Architecture, University of Trieste, Trieste, Italy, and ^hElettra – Sincrotrone Trieste S.p.A., Basovizza (Trieste), Italy. *Correspondence e-mail: yakov.nesterets@csiro.au

Results are presented of a recent experiment at the Imaging and Medical beamline of the Australian Synchrotron intended to contribute to the implementation of low-dose high-sensitivity three-dimensional mammographic phase-contrast imaging, initially at synchrotrons and subsequently in hospitals and medical imaging clinics. The effect of such imaging parameters as X-ray energy, source size, detector resolution, sample-to-detector distance, scanning and data processing strategies in the case of propagation-based phase-contrast computed tomography (CT) have been tested, quantified, evaluated and optimized using a plastic phantom simulating relevant breast-tissue characteristics. Analysis of the data collected using a Hamamatsu CMOS Flat Panel Sensor, with a pixel size of 100 μm , revealed the presence of propagation-based phase contrast and demonstrated significant improvement of the quality of phase-contrast CT imaging compared with conventional (absorption-based) CT, at medically acceptable radiation doses.

1. Introduction

Breast cancer is one of the two leading causes of cancer fatalities among women in most industrialized countries. This type of cancer can be very aggressive, with success of the treatment depending heavily on early detection which is currently the most important factor for reducing the morbidity and mortality of the patients. Therefore, health authorities in most countries recommend regular screening of women over 40 years of age, with two-dimensional (2D) X-ray mammography being the main screening and diagnostic technique used for this purpose at present.

Despite the intensive studies of the optimization of conventional (Johns & Yaffe, 1985) and phase-contrast (Zysk *et al.*, 2012) mammographic imaging systems, the main known problem with this technique is that it produces a relatively high percentage of both false-positive and false-negative results (Pisano *et al.*, 2005). A more recently introduced technique, digital tomosynthesis, generally delivers better results, mainly due to its three-dimensional (3D) imaging ability (multiple 2D slices through the breast) which reduces the effect of overlying breast tissue camouflaging focal breast masses (Ciatto *et al.*, 2013). However, due to its inherent



limitations, tomosynthesis cannot produce 3D images with the same image quality as computed tomography (CT) (Malliori *et al.*, 2012). Therefore, it is important to investigate the opportunities for 3D mammographic CT imaging that could satisfy the requirements of medical practice in terms of the dose delivered to the patient, the image quality and the costs.

It has been shown recently (Zhao *et al.*, 2012) that analyser-based CT (AB-CT) may allow 3D imaging of soft tissues and tumours at higher resolution and better contrast, and with a smaller radiation dose, compared with current clinical mammography. At the same time, recent theoretical and experimental studies (Diemoz *et al.*, 2012; Gureyev *et al.*, 2013, 2014a; Nesterets & Gureyev, 2014) have shown that, depending on the specific parameters of the experiment, alternative X-ray phase-contrast imaging methods, such as the propagation-based phase-contrast tomography (PB-CT), can deliver outcomes comparable with AB-CT with regard to image quality and dose, while being potentially simpler and cheaper to implement.

As a pre-requisite for successful translation of 3D phase-contrast mammography into clinical practice, it is essential to evaluate, quantify and optimize the main parameters of the PB-CT imaging technique, including the choice of X-ray energy, sample-to-detector distance, strategies for CT scans and the reconstruction techniques capable of maximizing the contrast-to-noise ratio (CNR) and suitable figures-of-merit (FOM) as a function of the X-ray dose delivered to the patient. While substantial progress has been achieved in this area in the last few years (Bravin *et al.*, 2013; Olivo *et al.*, 2013), there is still a great need for further research, testing and development before these techniques become suitable for routine clinical applications. The potential importance and value of optimized strategies for CT data acquisition and processing in phase-contrast imaging modalities have been clearly demonstrated in recent publications (Gureyev *et al.*, 2013, 2014a; Nesterets & Gureyev, 2014), unequivocally proving the existence of a significant potential for improvement in this field.

In our previous experiments at the SYRMEP beamline of the Elettra synchrotron in Trieste in 2013–2014 we performed multiple scans in AB-CT and PB-CT modes using plastic phantoms and several breast-tissue samples with normal and malignant tissues at different X-ray energies between 20 and 40 keV. These experiments have been very informative (Gureyev *et al.*, 2013, 2014a; Pacilè *et al.*, 2015), although an obvious limitation of these results was the inability to run similar tests at higher X-ray energies due to limitation on the energy range of the SYRMEP beamline. Note that according to some publications (*e.g.* Zhao *et al.*, 2012) the use of high-energy X-rays (60 keV and higher) can lead to further reduction of the dose and improvement of the corresponding CNR and FOM in the case of mammographic AB-CT. However, the corresponding energy dependence in the case of PB-CT has not been fully demonstrated experimentally yet, as far as we know. This question has been addressed during our recent experiment (which was carried out at X-ray energies up to 50 keV) at the Imaging and Medical beamline of the

Australian Synchrotron. The results of this experiment are presented below.

2. Experiment description

We have conducted in-line phase-contrast CT imaging experiments at the Imaging and Medical beamline of the Australian Synchrotron (Stevenson *et al.*, 2010). The detector used was a Hamamatsu CMOS Flat Panel Sensor C9252DK-14, utilized in partial scan mode, with pixel size $100\ \mu\text{m} \times 100\ \mu\text{m}$, 1174×99 pixels (H \times V) field of view and 12-bit output. The detector has a CsI scintillator directly deposited on a 2D photodiode array.

A specially designed and fabricated phantom was used in this experiment. A CT slice of the phantom is shown in Fig. 1. The phantom consists of a cylindrical block made of polycarbonate, with a diameter of 10 cm and height of 2 cm, having eight irregularly located cylindrical holes of 1 cm diameter, each filled with different substances as explained in the caption of Fig. 1. The chemical composition and mass density for the substances constituting the phantom are contained in Table 1.

The sample was imaged with monochromatic X-rays at three energies: 38 keV, 45 keV and 50 keV. While the source-to-detector distance, R , was fixed to about 142.5 m, the sample rotation-axis to detector distance (sample-to-detector distance, for short), R_2 , was set to one of four values: 27 cm, 1 m, 2 m and 5 m. Table 2 lists the corresponding geometrical magnifications of the imaging setups, M , and the effective pixel size of the detector, h . Thus the total number of different imaging configurations was 12. For each configuration, eight 360° scans [four 180° scans for two configurations, (45 keV, 5 m) and (50 keV, 5 m)] were collected, with an angular step of approximately 0.1° . For each individual CT scan, 40 dark-field images and 40 flat-field images were collected, half before and half after a sample scan.

3. Results and discussion

CT data analysis (including pre-processing of data, CT reconstruction and optional post-processing) was carried out using *X-TRACT* software (X-TRACT, 2015; Gureyev *et al.*, 2011; Thompson *et al.*, 2011).

For each individual CT scan the pre-processing of image data consisted of three main steps: (i) zinger (hot pixel) filtering of all images, (ii) subtraction of the average dark field from the corresponding average flat field and from individual sample projections, and (iii) division of the dark-field-corrected individual sample projections by the dark-field-corrected average flat field. After pre-processing, the normalized projections were converted to sinograms.

CT reconstruction of the imaginary part, β , of the X-ray complex refractive index $n = 1 - \delta + i\beta$, unless otherwise stated, was carried out using a GPU-accelerated implementation (Nesterets & Gureyev, 2009) of conventional parallel-beam filtered back-projection (FBP) algorithm utilizing a ramp filter.

Table 1
Chemical composition and mass densities of the materials present or emulated in the phantom.

Substance	Composition (formula or weight %)	Mass density at 293 K (g cm ⁻³)	
Polycarbonate	C ₁₆ H ₁₄ O ₃	1.2	
Glycerol	C ₃ H ₈ O ₃	1.261	
Calcium chloride 1 M	Ca	3.69	
	Cl	6.53	
	H	10.05	
	O	79.73	
			1.086
Ethanol 35v%	H	11.75	
	C	15.07	
	O	73.18	
Paraffin oil	H	14.86	
	C	85.14	
Water	H ₂ O	1	
Gland tissue†	H	10.2	
	C	18.4	
	N	3.2	
	O	67.7	
	S	0.125	
	P	0.125	
	K	0.125	
	Ca	0.125	
	Adipose tissue†	H	11.2
		C	61.9
		N	1.7
		O	25.1
		S	0.025
P		0.025	
K		0.025	
Ca		0.025	
Glandular tissue (50 w% adipose, 50 w% glandular)		H	10.7
		C	40.15
		N	2.45
		O	46.4
		P	0.075
	S	0.075	
	K	0.075	
	Ca	0.075	

† Hammerstein *et al.* (1979).

The post-processing step consisted of ring-removal filtering of the reconstructed axial CT slices using an implementation of the algorithm proposed by Sijbers & Postnov (2004).

A single representative axial CT slice was chosen (from the stack of 99 slices) for comparison of different experimental

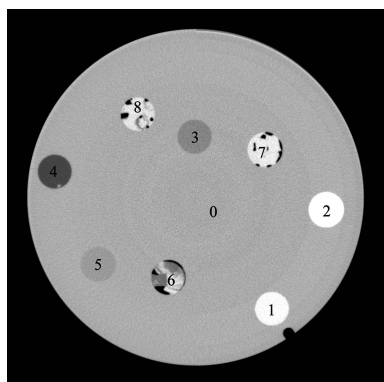


Figure 1
Composition of the phantom used in the experiment. 0: polycarbonate; 1: glycerol; 2: calcium chloride (1 M); 3: ethanol (35v%); 4: paraffin oil; 5: water; 6: fatty ham; 7: meaty ham; 8: fibrous ham.

Table 2
Geometrical parameters for different experimental configurations.

Values in parentheses represent errors in the least significant digit.

R (m)	R_2 (m)	M^\dagger	h^\ddagger (μm)
142.5 (5)	0.27	1.001898 (7)	99.8106 (7)
	1	1.00707 (3)	99.298 (2)
	2	1.01423 (5)	98.597 (5)
	5	1.0364 (1)	96.49 (1)

† $M \equiv R/(R - R_2)$ is the geometrical magnification. ‡ h is the pixel size in the reconstructed slice. Due to magnification, this size is smaller than the detector pixel size.

Table 3
Values of the parameter $R_{\text{abs},r}$ used in dose calculations, for different parameters of the phantom shown in Fig. 4.

R_{out} (cm)	r (cm)	$R_{\text{abs},r}$		
		38 keV	45 keV	50 keV
3	2.5	0.20271	0.14886	0.12579
4	3.5	0.28496	0.21688	0.18557
5	4.5	0.35841	0.27961	0.24279

configurations and conditions. The results of the CT reconstruction process described above, for 12 experimental configurations, using all available projection data (see §2 for details) are presented in Figs. 2 and 3. Detailed analysis of these results, in terms of the reconstruction accuracy, is carried out below, in §3.2. The effect of in-line phase contrast on CT reconstruction is discussed in §3.3. In §3.4, we evaluate the quality of CT reconstructions using several quality measures. In view of application to mammography, most of the quality measures are dose-normalized. For this reason, we begin our analysis by estimating, in §3.1, the mean glandular dose (MGD) for individual projection images, for different experimental conditions.

3.1. Radiation dose estimations

Using the breast phantom schematically depicted in Fig. 4 (NCRP, 2004; Dance, 1990), the mean absorbed dose (in mGy) of the glandular tissue, having radius r (in cm) and located inside a cylinder of radius R_{out} (in cm), consisting of adipose tissue (fat), simulating the skin layer, can be calculated as follows (Johns & Yaffe, 1985; Nesterets & Gureyev, 2014):

$$D_{\text{abs}} [\text{mGy}] = (2/\pi) 1.602 \times 10^{-10} \times \frac{R_{\text{out}} [\text{cm}]}{r^2 [\text{cm}^2]} \frac{R_{\text{abs},r} F [\text{photons cm}^{-2}] E [\text{keV}]}{\rho_r [\text{g cm}^{-3}]}. \quad (1)$$

Here, E is the X-ray energy (in keV), F is the incident photon fluence (in photons cm⁻²), ρ_r is the mass density of the glandular tissue (in g cm⁻³) and $R_{\text{abs},r}$ is the fraction of X-ray energy incident on the phantom and absorbed in the glandular tissue. The latter was calculated using Monte Carlo (MC) simulations and the results are shown in Fig. 5 and in Table 3. The chemical compositions for the skin layer and glandular tissue used in the MC simulations are presented in Table 1.

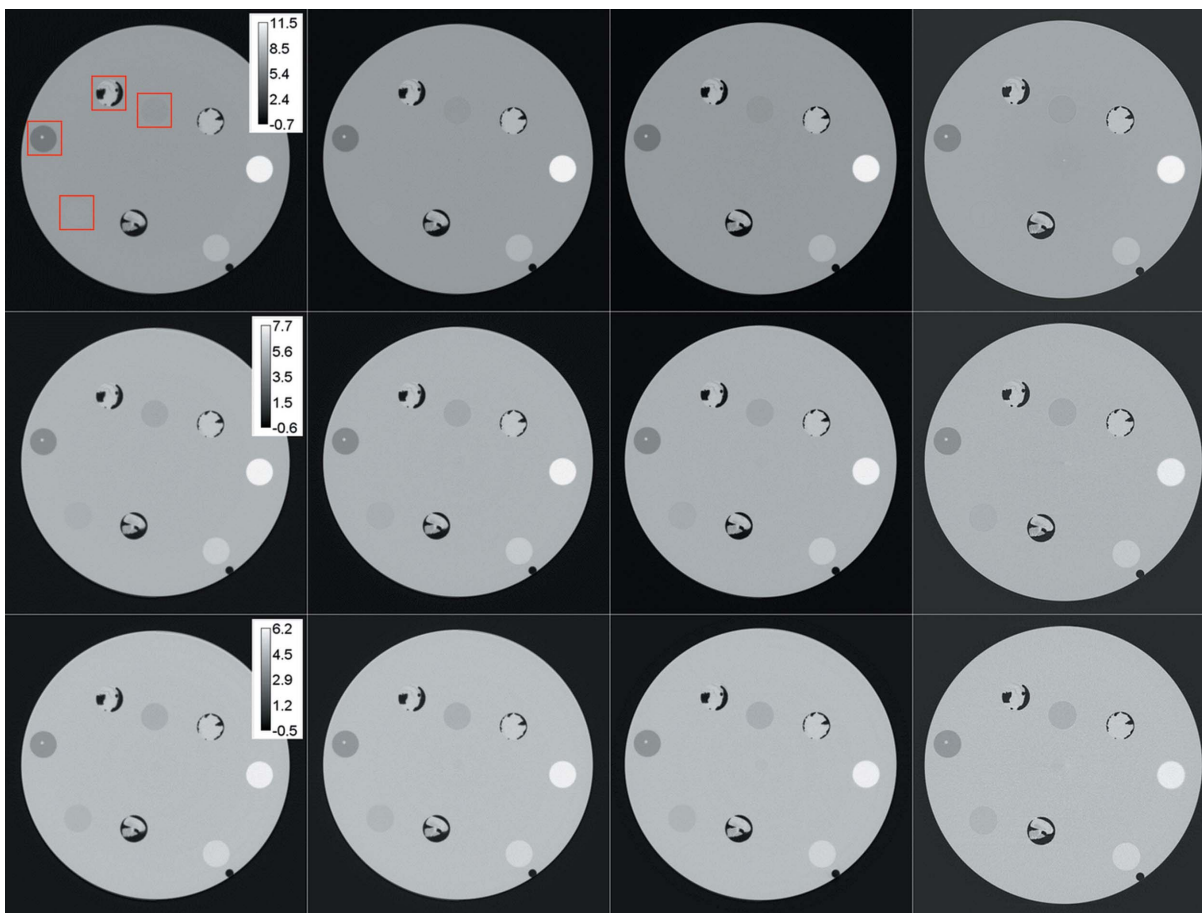


Figure 2 FBP CT reconstructions of the imaginary part, β , of the X-ray complex refractive index using the full sets of 28920 projections [7232 projections for two configurations, (45 keV, 5 m) and (50 keV, 5 m)], for 12 combinations of the sample-to-detector distance and X-ray energy. Left to right: 0.27 m, 1 m, 2 m, 5 m; top to bottom: 38 keV, 45 keV, 50 keV. The calibration bars in the left-most plots show $\beta \times 10^{11}$.

During the experiment, an ion chamber (IC) was installed in the X-ray beam upstream from the sample, at a distance of about 136.2 m from the source. The readings from the IC were recorded during CT data acquisition. These readings have been used for measuring the photon fluence rate and the corresponding rate of the surface absorbed dose to air, DR_{IC} , at the IC plane. Taking into account the exposure time of 33 ms for each individual projection, the photon fluences per individual projection image, in the IC plane, F_{IC} , for each of 12 CT scans, have been calculated and the values are contained in the third column of Table 4. The latter values were used for calculating the corresponding incident photon fluences in the sample plane, F_{smp} (the third last column in Table 4), by taking into account the attenuation of the X-ray beam by an air gap between the IC and the sample, as well as the geometrical magnification of the X-ray beam between the IC and the sample. Similarly, the surface absorbed doses to air at the sample plane, D_{smp} , were calculated. Using equation (1), the photon fluences in the sample plane were converted into MGDs per individual projection image, for the phantom having inner and outer radii of 4.5 cm and 5 cm, respectively. The calculated MGDs are contained in the last column of Table 4.

Comparison of the last two columns in Table 4 shows that the surface dose to air, D_{smp} , is consistently bigger than the calculated MGD, especially for lower energies. This is partially due to the shielding effect of the skin layer and also due to the nature of the MGD which quantifies an average X-ray energy absorbed in the glandular tissue.

3.2. Accuracy of the quantitative CT reconstruction

Tables 5 and 6 show the theoretical, β_{theor} , and the experimental, β_{exp} , values of the imaginary part of the complex refractive index, for materials constituting the phantom, for several selected experimental configurations. The experimental values were measured in CT slices reconstructed from the full set of 28920 projections (see §2).

Analysis of the data contained in Tables 5 and 6 indicates that, in general, the experimentally measured β -values [and the associated linear attenuation coefficients $\mu \equiv (4\pi/\lambda)\beta$] are consistently smaller (by about 1–3%) than the theoretical values. The only exception is the ethanol solution for which the experimental β -value is slightly larger than the theoretical one. This can be explained by a slightly smaller concentration of ethanol compared with the nominal concentration of

Table 4

Incident photon fluences (per single projection) and the corresponding mean glandular absorbed doses calculated, using equation (1), for the cylindrical numerical phantom shown in Fig. 4 (with outer radius $R_{out} = 5$ cm and inner radius $r = 4.5$ cm).

Energy (keV)	R_2 (m)	$F_{IC}^\dagger \times 10^{-7}$ (photons cm^{-2})	DR_{IC}^\ddagger (mGy s^{-1})	Δz^\S (m)	T_{air}^\P	m^\ddagger	$F_{smp}^{\ddagger\ddagger} \times 10^{-7}$ (photons cm^{-2})	$D_{smp}^{\S\S}$ (μGy)	$D_{abs}^{\P\P}$ (μGy)
38	0.27	8.59 (3)	1.250 (4)	6.0 (5)	0.83 (1)	1.044 (4)	6.5 (1)	31.3 (5)	22.8 (4)
	1	8.29 (3)	1.208 (4)	5.3 (5)	0.85 (1)	1.039 (4)	6.5 (1)	31.2 (5)	22.7 (4)
	2	9.00 (3)	1.311 (5)	4.3 (5)	0.87 (1)	1.032 (4)	7.4 (1)	35.5 (6)	25.8 (5)
	5	9.10 (3)	1.390 (5)	1.3 (5)	0.96 (2)	1.010 (4)	8.6 (2)	43.2 (8)	30.0 (5)
45	0.27	6.12 (2)	0.775 (3)	6.0 (5)	0.85 (1)	1.044 (4)	4.77 (8)	19.9 (3)	15.4 (2)
	1	6.19 (2)	0.704 (3)	5.3 (5)	0.87 (1)	1.039 (4)	4.96 (8)	18.6 (3)	16.0 (3)
	2	6.06 (1)	0.690 (2)	4.3 (5)	0.89 (1)	1.032 (4)	5.07 (8)	19.0 (3)	16.4 (3)
	5	7.04 (2)	0.801 (3)	1.3 (5)	0.97 (1)	1.010 (4)	6.7 (1)	25.0 (4)	21.5 (4)
50	0.27	5.25 (2)	0.522 (2)	6.0 (5)	0.86 (1)	1.044 (4)	4.14 (6)	13.6 (2)	12.9 (2)
	1	5.27 (2)	0.523 (2)	5.3 (5)	0.87 (1)	1.039 (4)	4.27 (6)	14.0 (2)	13.3 (2)
	2	5.33 (2)	0.531 (2)	4.3 (5)	0.90 (1)	1.032 (4)	4.49 (7)	14.8 (2)	14.0 (2)
	5	6.14 (2)	0.610 (2)	1.3 (5)	0.97 (1)	1.010 (4)	5.83 (9)	19.1 (3)	18.2 (3)

$\dagger F_{IC}$ is the photon fluence in the ion chamber plane. This takes into account the electron-loss correction: 1.31, 1.42 and 1.45 for 38 keV, 45 keV and 50 keV, respectively. The exposure time per single projection, t_{exp} , was 33 ms. $\ddagger DR_{IC}$ is the surface dose rate in the IC plane, calculated using the IC readings. This takes into account the above electron-loss correction. $\S \Delta z$ is the distance between the ion chamber and the sample. $\P T_{air}$ is the transmittance of the air gap having thickness Δz . $\ddagger m$ is the geometrical magnification between the ion chamber plane (located at the distance $R_{IC} = 136.2$ m from the source) and the sample plane (located at the distance $R_{IC} + \Delta z$ from the source), $m = 1 + \Delta z/R_{IC}$. $\ddagger\ddagger F_{smp}$ is the photon fluence in the sample plane: $F_{smp} = F_{IC} T_{air} / m^2$. $\S\S D_{smp}$ is the surface dose to air in the sample plane: $D_{smp} = DR_{IC} t_{exp} T_{air} / m^2$. $\P\P D_{abs}$ is the mean glandular absorbed dose (per single projection) and is calculated using equation (1) and the values of the parameter $R_{abs,r}$ from the last row of Table 3.

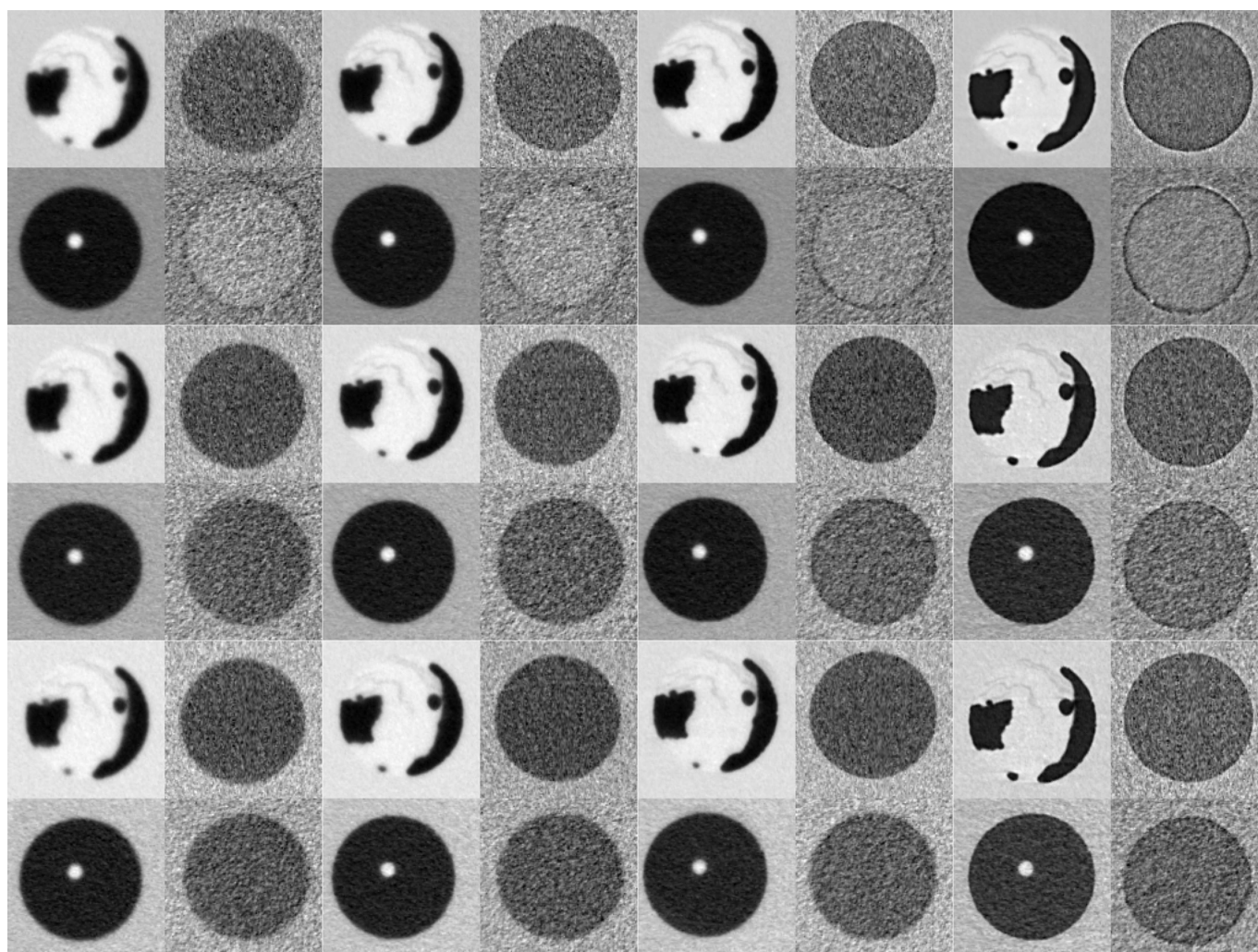


Figure 3

Enlarged fragments of the reconstructed slices shown in Fig. 2 corresponding to the inserts 8, 3, 4 and 5 of the phantom (see Fig. 1 for details) and indicated by square boxes shown in the top-left image in Fig. 2. For each fragment the image histogram was adjusted to the fragment's minimum and maximum values.

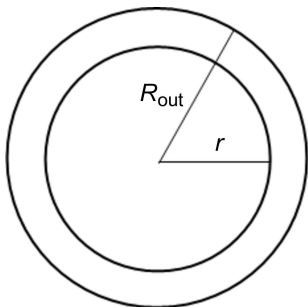


Figure 4
Schematic diagram of the numerical phantom used for mean glandular dose calculations.

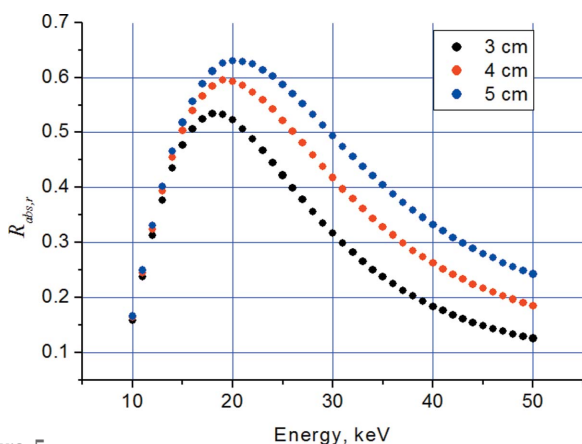


Figure 5
Energy dependencies of the parameter $R_{abs,r}$ specifying the fraction of the X-ray energy incident on the phantom, shown in Fig. 4, and absorbed in the glandular tissue forming a cylinder of radius r , for different radii of the phantom (see also text in §3.1).

35 volume percent (35v%). Also, for paraffin oil, the mass density, as provided by the manufacturer, was in the range $0.827\text{--}0.890\text{ g cm}^{-3}$. As a result, Tables 5 and 6 contain the corresponding ranges for the theoretical β -values, and the experimentally measured β -values are well within these ranges.

It is also worth mentioning that the β -values of polycarbonate were observed to slightly vary (by up to about 2% from the average value) across the reconstructed CT slices (note that in Tables 5 and 6 the values without brackets were measured near the centre of the reconstructed slices while the values in the square brackets were measured near the edge of the slices). Moreover, the degree of this non-uniformity was different for different experimental conditions (X-ray energy and/or sample-to-detector distance).

Fig. 6 shows experimental β -values obtained from CT scans collected at a sample-to-detector distance of 2 m, plotted against the theoretical energy dependencies of the corresponding β -values, for some materials constituting the phantom.

3.3. Phase contrast observation

It should be emphasized that the CT slices presented in Fig. 2 were deliberately reconstructed without phase retrieval.

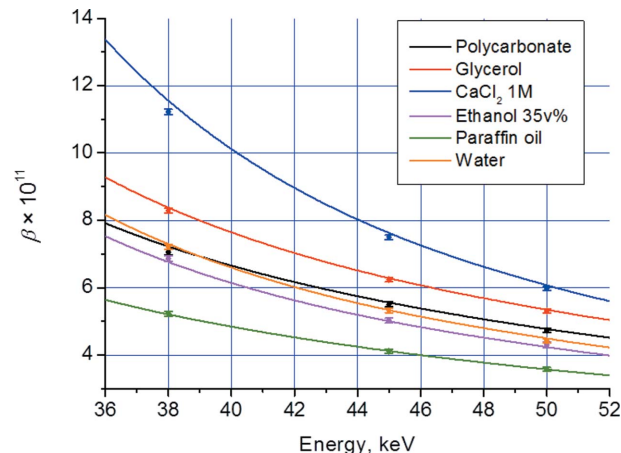


Figure 6
Theoretical (solid lines) and experimentally measured (dots) values of the imaginary part of the complex refractive index, for some materials constituting the phantom. Experimental points correspond to the full set of 28920 projections collected at a sample-to-detector distance of 2 m. A mass density of 0.86 g cm^{-3} was used for paraffin oil (see Table 1).

As a result, in-line phase contrast manifests itself as edge enhancement in these slices. In order to make it easier for the reader to observe this effect, Fig. 3 shows enlarged fragments of the slices delineated in the top-left image of Fig. 2 using square boxes. Analysis of Fig. 3 indicates that in the case of the smallest sample-to-detector distance (0.27 m) the features of the phantom have visibly smeared edges (see the first column in Fig. 3). By increasing the sample-to-detector distance, one can first clearly observe edge sharpness improvement (see the second and third columns in Fig. 3) and eventually the appearance of phase-contrast fringes which are most pronounced at 5 m sample-to-detector distance (see the fourth column in Fig. 3).

Whereas the phase contrast increases with increasing sample-to-detector distance, it decreases with increasing X-ray energy. This can be explained using the transport of intensity equation (TIE) (Teague, 1983):

$$I_{R'}(x, y; \lambda) = I_0(x, y; \lambda) - R'\lambda/(2\pi) \nabla \cdot [I_0(x, y; \lambda) \nabla \varphi_0(x, y; \lambda)], \quad (2)$$

where $I_{R'}(x, y; \lambda)$ and $I_0(x, y; \lambda) = I_{in}(x, y; \lambda) \exp[-(4\pi/\lambda) \int \beta(x, y, z; \lambda) dz]$ are the intensity distributions in the image and the object planes, respectively, $\varphi_0(x, y; \lambda) = \varphi_{in}(x, y; \lambda) - (2\pi/\lambda) \int \delta(x, y, z; \lambda) dz$ is the phase distribution in the object plane, $I_{in}(x, y; \lambda)$ and $\varphi_{in}(x, y; \lambda)$ are the intensity and phase distributions in the illuminating beam, and R' is the effective propagation distance. According to the TIE, the magnitude of the phase contrast at any boundary is proportional to the effective propagation distance R' (which, in the case of large source-to-sample distances, is accurately approximated by the sample-to-detector distance R_2) and to the real decrement $(\delta_1 - \delta_2)$ of the relative complex refractive index for two materials forming the boundary. For hard X-rays, the real decrement δ of the refractive index for any material decreases with increasing X-ray energy. Analysis of Figs. 2 and 3 shows that, as expected, the phase-contrast effects become weaker

Table 5

Theoretical, β_{theor} , and experimental, β_{exp} , values of the imaginary part of the complex refractive index for materials constituting the phantom (see Fig. 1 for details), for the three X-ray energies used in the experiment.

The experimental values were measured in CT slices reconstructed from the full set of 28920 projections collected at a sample-to-detector distance of 2 m. For polycarbonate, values without brackets were measured near the centre of the reconstructed slices while values in square brackets were measured near the edge of the slices.

Index	Material	$E = 38 \text{ keV}$			$E = 45 \text{ keV}$			$E = 50 \text{ keV}$		
		$\beta_{\text{theor}} \times 10^{11}$	$\beta_{\text{exp}} \times 10^{11}$	$\beta_{\text{exp}} / \beta_{\text{theor}}$	$\beta_{\text{theor}} \times 10^{11}$	$\beta_{\text{exp}} \times 10^{11}$	$\beta_{\text{exp}} / \beta_{\text{theor}}$	$\beta_{\text{theor}} \times 10^{11}$	$\beta_{\text{exp}} \times 10^{11}$	$\beta_{\text{exp}} / \beta_{\text{theor}}$
0	Polycarbonate	7.225	7.1 (1) [7.18 (8)]	0.99 (2) [0.99 (1)]	5.560	5.49 (8) [5.52 (6)]	0.99 (2) [0.99 (1)]	4.774	4.72 (7) [4.74 (6)]	0.99 (2) [0.99 (1)]
1	Glycerol	8.380	8.29 (8)	0.99 (1)	6.283	6.24 (7)	0.99 (1)	5.346	5.31 (6)	0.99 (1)
2	CaCl ₂ 1 M	11.557	11.18 (9)	0.968 (8)	7.625	7.50 (7)	0.983 (9)	6.073	5.98 (6)	0.99 (1)
3	Ethanol 35v%	6.764	6.9 (1)	1.02 (2)	5.004	5.10 (8)	1.02 (2)	4.237	4.30 (7)	1.01 (2)
4	Paraffin oil	5.007–5.389	5.23 (7)	–	3.960–4.261	4.11 (6)	–	3.436–3.698	3.57 (6)	–
5	Water	7.296	7.21 (8)	0.99 (1)	5.333	5.32 (7)	1.00 (1)	4.495	4.48 (6)	1.00 (1)
6	Fatty ham	–	6.1 (1)	–	–	4.68 (8)	–	–	4.02 (8)	–
7	Meaty ham	–	8.5 (1)	–	–	6.12 (9)	–	–	5.06 (7)	–
8	Fibrous ham	–	8.5 (1)	–	–	6.04 (9)	–	–	5.01 (7)	–

Table 6

Theoretical, β_{theor} , and experimental, β_{exp} , values of the imaginary part of the complex refractive index for materials constituting the phantom (see Fig. 1 for details), for three sample-to-detector distances.

The experimental values were measured in CT slices reconstructed from the full set of 28920 projections collected at an X-ray energy of 38 keV. For polycarbonate, values without brackets were measured near the centre of the reconstructed slices while values in square brackets were measured near the edge of the slices.

Index	Material	$\beta_{\text{theor}} \times 10^{11}$	$R_2 = 0.27 \text{ m}$		$R_2 = 1 \text{ m}$		$R_2 = 5 \text{ m}$	
			$\beta_{\text{exp}} \times 10^{11}$	$\beta_{\text{exp}} / \beta_{\text{theor}}$	$\beta_{\text{exp}} \times 10^{11}$	$\beta_{\text{exp}} / \beta_{\text{theor}}$	$\beta_{\text{exp}} \times 10^{11}$	$\beta_{\text{exp}} / \beta_{\text{theor}}$
0	Polycarbonate	7.225	7.0 (1) [7.14 (7)]	0.97 (1) [0.99 (1)]	7.2 (1) [7.17 (8)]	0.99 (1) [0.99 (1)]	7.0 (1) [7.18 (8)]	0.97 (2) [0.99 (1)]
1	Glycerol	8.380	8.23 (8)	0.982 (9)	8.28 (8)	0.988 (9)	8.30 (8)	0.99 (1)
2	CaCl ₂ 1 M	11.557	11.09 (9)	0.960 (8)	11.21 (8)	0.970 (7)	11.20 (9)	0.969 (8)
3	Ethanol 35v%	6.764	6.81 (9)	1.01 (1)	6.9 (1)	1.02 (1)	6.8 (1)	1.01 (2)
4	Paraffin oil	5.007–5.389	5.21 (7)	–	5.23 (7)	–	5.22 (7)	–
5	Water	7.296	7.17 (8)	0.98 (1)	7.23 (8)	0.99 (1)	7.20 (9)	0.99 (1)
6	Fatty ham	–	6.0 (1)	–	6.1 (1)	–	6.1 (2)	–
7	Meaty ham	–	8.4 (1)	–	8.5 (1)	–	8.5 (1)	–
8	Fibrous ham	–	8.3 (1)	–	8.4 (1)	–	8.5 (1)	–

when the X-ray energy increases. In particular, this becomes apparent if one compares fragments in the top element of the right-most column with the corresponding fragments of the other two elements of that column (the rows correspond to X-ray energy of 38 keV, 45 keV and 50 keV, respectively).

Remarkably, in-line phase contrast, clearly observed at a sample-to-detector distance of 5 m, is quite significant despite the relatively large effective pixel size of the detector, about 100 μm , and the large horizontal source size, about 800 μm (note, however, that the effective source size in the detector plane is significantly smaller, by a factor of about 5/142). In order to quantify the effect of in-line phase contrast on the sharpness of the edges of the phantom features we measured their width using the following approach. First we selected linear profiles across the boundaries between the inserts and the polycarbonate cylinder in CT slices which were four-fold over-sampled using linear interpolations. Then, these profiles were fitted with a sigmoidal function resulting from a convolution of

Table 7

Widths (in μm) of the boundaries between polycarbonate and three selected materials, in CT slices reconstructed using the FBP algorithm, applied to the full set of 28920 projections at 38 keV, and with post-reconstruction ring filtering.

Values without parentheses correspond to raw projections while values in parentheses correspond to phase-retrieved projections (TIE-HOM with $\gamma = 1000$).

Material	Width (μm)			
	$R_2 = 0.27 \text{ m}$	$R_2 = 1 \text{ m}$	$R_2 = 2 \text{ m}$	$R_2 = 5 \text{ m}$
Glycerol	526 \pm 20	323 \pm 19 (371 \pm 15)	333 \pm 20 (399 \pm 12)	242 \pm 16 (414 \pm 9)
CaCl ₂ 1 M	499 \pm 8	468 \pm 7 (495 \pm 4)	477 \pm 6 (553 \pm 4)	492 \pm 7 (626 \pm 3)
Paraffin oil	425 \pm 9	347 \pm 8 (382 \pm 6)	344 \pm 9 (425 \pm 6)	185 \pm 8 (355 \pm 4)

a sharp edge profile with a Gaussian point spread function (PSF), $f(x) = a + b \text{erf}[(x - c)/(2^{1/2}\sigma)]$ (a , b , c and σ are the fitting parameters). The full width at half-maximum (FWHM) of the Gaussian PSF, 2.3548σ , was considered as the width of the edge.

The widths of the boundaries between polycarbonate and three selected materials, *i.e.* glycerol, calcium chloride and paraffin oil, are given in Table 7. As expected, the width of the edges in the reconstructed CT slices usually decreases with increasing sample-to-detector distance (Gureyev *et al.*, 2004).

Moreover, for a fixed sample-to-detector distance, the edge sharpness improvement strongly depends on the X-ray optical properties of the neighbouring materials, namely, on the ratio $(\delta_1 - \delta_2)/(\beta_1 - \beta_2)$. Theoretical values for this ratio, for several material combinations, are provided in Table 8. In particular, amongst the three materials, the edge sharpness improvement was the biggest for paraffin oil, for which the ratio was the biggest. On the other hand, for calcium chloride, for which the ratio is negative, the edge sharpness was almost constant with increasing sample-to-detector distance.

3.4. Effect of phase retrieval on the quality of CT reconstruction

It is well acknowledged that phase retrieval using an algorithm based on the homogeneous transport of intensity equation (TIE-HOM) (Paganin *et al.*, 2002),

$$I_R(x, y; \lambda) = [1 - R' \lambda \gamma / (4\pi) \nabla^2] I_0(x, y; \lambda), \quad (3)$$

results, in general, in reduced noise in reconstructed CT slices while preserving the sharpness of the edges when used with a proper parameter γ quantifying the relationship between the real and imaginary parts of the decrement of the refraction index of the object (see, for example, Beltran *et al.*, 2011; Nesterets & Gureyev, 2014). We applied the TIE-HOM algorithm [which corresponds to inversion of equation (3)] to projection data sets and subsequently carried out FBP CT reconstruction. In order to restrict the absorbed dose to values currently accepted for standard mammographic screening, we restricted the number of projections to 361 over 180° (this is an 80-fold reduction compared with the high photon statistics data used for CT reconstructions shown in Figs. 2 and 3). The

Table 8

Values of the ratio $(\delta_1 - \delta_2)/(\beta_1 - \beta_2)$ for different material combinations and X-ray energies of interest.

Material combination	Ratio $(\delta_1 - \delta_2)/(\beta_1 - \beta_2)$		
	$E = 38 \text{ keV}$	$E = 45 \text{ keV}$	$E = 50 \text{ keV}$
Glycerol/polycarb.	1302	1483	1519
CaCl ₂ /polycarb.	-245	-368	-474
Ethanol 35v%/polycarb.	6176	3649	3066
Paraffin oil†/polycarb.	1992	1987	1933
Water/polycarb.	-31098	6951	4592
Polycarb./air	2516	2331	2199
Gland/adipose	1083	1268	1328

† Mass density 0.86 g cm⁻³ was used in calculations.

MGDs, D , per complete CT scans, were calculated using the dose values per single projection, from the last column of Table 4, and multiplying them by the number of projections in a CT scan. For a 361-projection CT scan, D was between 4.7 mGy and 10.8 mGy, depending on the imaging parameters.

In this paper, our primary target is mammographic CT. In the case of breast tissue its main components are gland and adipose tissues. According to Table 8, in the X-ray energy range from 38 keV to 50 keV the ratio $(\delta_1 - \delta_2)/(\beta_1 - \beta_2)$ for the gland/adipose pair is slightly larger than 1000. For this reason, the parameter γ in the TIE-HOM-based phase-retrieval algorithm was set to 1000 for all three energies. One reconstructed CT slice, corresponding to an X-ray energy of 38 keV, for four values of the sample-to-detector distance, is shown in Fig. 7 together with its magnified fragments.

In order to quantify the quality of the reconstructions in the presence of noise we utilized the quality index recently introduced by Gureyev *et al.* (2014a,b). The results of this

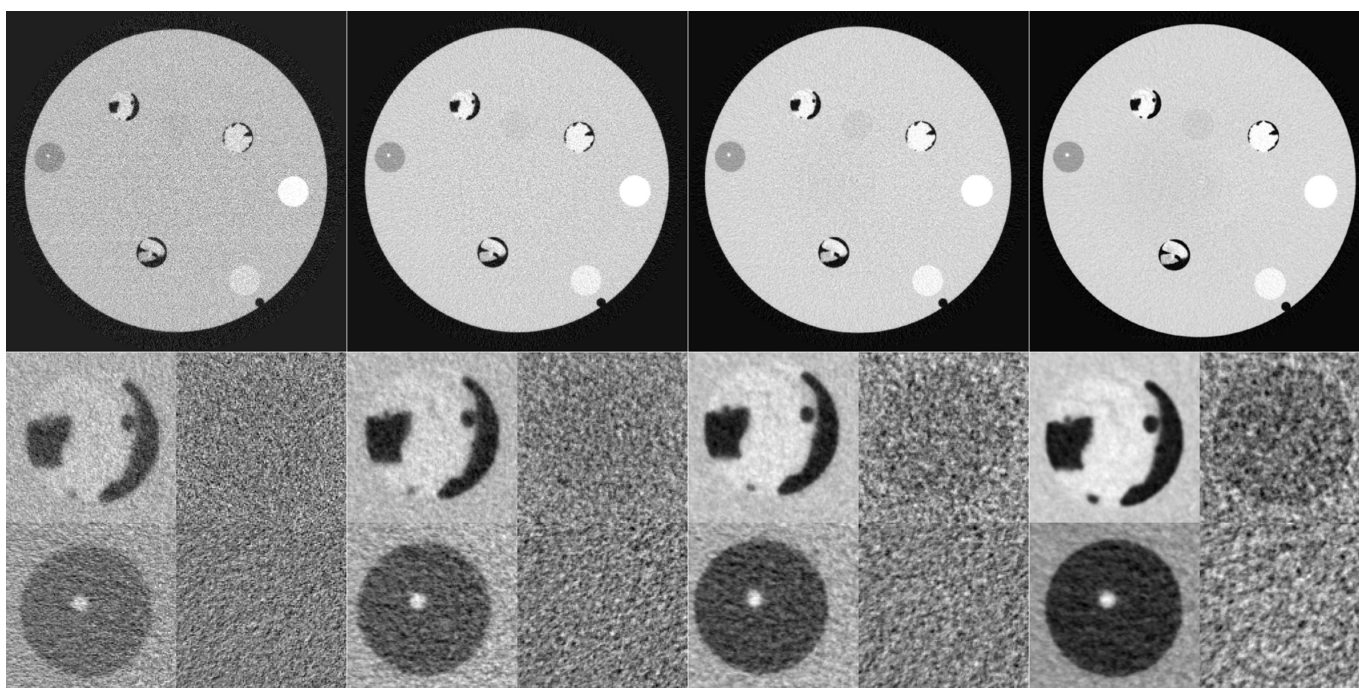


Figure 7 Effect of phase retrieval (TIE-HOM with $\gamma = 1000$) on FBP CT reconstruction from low-photon-statistics data (361 projections over 180°), at 38 keV X-ray energy, for different sample-to-detector distances. From left to right: 0.27 m, 1 m, 2 m and 5 m.

Table 9

Quality characteristics of CT slices reconstructed (using FBP) from phase-retrieved (using TIE-HOM with $\gamma = 1000$) low-photon-statistics (361 projections) data at X-ray energy $E = 38$ keV, for different sample-to-detector distances.

Index	Material	$R_2 = 0.27$ m†			$R_2 = 1$ m		
		SNR / $D^{1/2}$ (mGy $^{-1/2}$)	Res (μ m)	$Q_S \ddagger \times 10^4$ (μ m $^{-1}$ mGy $^{-1/2}$)	SNR / $D^{1/2}$ (mGy $^{-1/2}$)	Res (μ m)	$Q_S \times 10^4$ (μ m $^{-1}$ mGy $^{-1/2}$)
0	Polycarbonate	1.73 ± 0.02 [2.25 ± 0.02]	141.4 [142.5]	122 ± 1 [157 ± 1]	3.46 ± 0.03 [4.49 ± 0.04]	159.7 [157.9]	217 ± 2 [284 ± 2]
1	Glycerol	2.54 ± 0.02	142.1	179 ± 2	5.33 ± 0.04	160.0	333 ± 3
2	CaCl ₂ 1 M	3.14 ± 0.03	141.7	222 ± 2	6.16 ± 0.05	160.9	383 ± 3
3	Ethanol 35v%	1.81 ± 0.02	141.2	128 ± 1	3.66 ± 0.03	158.0	232 ± 2
4	Paraffin oil	1.83 ± 0.02	143.4	127 ± 1	3.58 ± 0.03	162.3	221 ± 2
5	Water	2.23 ± 0.02	142.5	156 ± 1	4.43 ± 0.04	160.4	276 ± 2
6	Fatty ham	1.72 ± 0.02	136.2	126 ± 1	3.52 ± 0.03	155.2	227 ± 2
7	Meaty ham	2.21 ± 0.02	140.1	157 ± 1	4.44 ± 0.04	153.7	289 ± 2
8	Fibrous ham	2.31 ± 0.02	139.6	165 ± 1	4.69 ± 0.04	155.1	303 ± 3

Index	Material	$R_2 = 2$ m			$R_2 = 5$ m		
		SNR / $D^{1/2}$ (mGy $^{-1/2}$)	Res (μ m)	$Q_S \times 10^4$ (μ m $^{-1}$ mGy $^{-1/2}$)	SNR / $D^{1/2}$ (mGy $^{-1/2}$)	Res (μ m)	$Q_S \times 10^4$ (μ m $^{-1}$ mGy $^{-1/2}$)
0	Polycarbonate	4.71 ± 0.04 [5.82 ± 0.05]	166.7 [168.4]	283 ± 2 [346 ± 3]	6.98 ± 0.06 [8.03 ± 0.07]	173.5 [176.5]	402 ± 3 [455 ± 4]
1	Glycerol	6.84 ± 0.06	168.2	406 ± 4	10.01 ± 0.09	173.9	576 ± 5
2	CaCl ₂ 1 M	8.43 ± 0.07	167.2	504 ± 4	11.4 ± 0.1	175.6	651 ± 6
3	Ethanol 35v%	4.67 ± 0.04	167.0	280 ± 2	6.73 ± 0.06	174.8	385 ± 3
4	Paraffin oil	4.64 ± 0.04	169.6	274 ± 2	6.64 ± 0.06	177.5	374 ± 3
5	Water	5.88 ± 0.05	166.4	353 ± 3	8.18 ± 0.07	174.2	469 ± 4
6	Fatty ham	4.90 ± 0.04	158.2	309 ± 3	5.55 ± 0.05	176.0	316 ± 3
7	Meaty ham	6.15 ± 0.05	158.9	387 ± 3	7.90 ± 0.07	170.9	463 ± 4
8	Fibrous ham	5.97 ± 0.05	163.5	365 ± 3	8.83 ± 0.07	167.3	528 ± 4

† No phase retrieval. ‡ $Q_S = \text{SNR} / D^{1/2} / \text{Res}$.

analysis are summarized in Tables 9 and 10 which contain values of three parameters characterizing the image quality including the signal-to-noise ratio (SNR) per unit dose, $\text{SNR}/D^{1/2}$, the spatial resolution and the ratio of the two which we use as the modified quality index, Q_S , in this paper.

Both the SNR and the spatial resolution have been calculated using a uniform region inside each feature of the phantom. The SNR was defined as the ratio of the mean β -value in the region to its standard deviation. The resolution was estimated by calculating the noise power spectrum in the region and evaluating the inverse of its second moment's square root. Note that the thus defined resolution can only be used to accurately estimate the characteristic length scale of spatially correlated noise. This characteristic of noise is complementary to its standard deviation and, in general, these two cannot be improved simultaneously (see, for example, Gureyev *et al.*, 2014b). We should emphasize that it is this definition of spatial resolution that is used below, in our quantitative analysis.

We also calculated the conventional contrast-to-noise ratio (CNR),

$$\text{CNR} = \frac{|\langle \beta_1 \rangle - \langle \beta_2 \rangle|}{\{[\text{var}(\beta_1) + \text{var}(\beta_2)]/2\}^{1/2}}, \quad (4)$$

which quantifies the ability to differentiate materials in the sample. Here the angular brackets and $\text{var}(\dots)$ designate the mean value and the variance of a spatial distribution,

respectively. In our subsequent data analysis we evaluate the CNR per unit dose, $\text{CNR}/D^{1/2}$, and (where available) the width of the boundaries between polycarbonate and inserts, FWHM, as well as the figure-of-merit, FOM, defined as the ratio of the CNR per unit dose to the width of the boundaries.

First, we investigate the effect of the sample-to-detector distance on the quality of CT slices reconstructed with the conventional FBP algorithm, using the quality measures defined above.

Analysis of the data in Table 9 shows that, with increasing sample-to-detector distance (within the range used in the experiment), the SNR per unit dose as well as the quality index are monotonically increasing, for all materials constituting the phantom. For SNR this is an expected behaviour due to the nature of the TIE-HOM algorithm. Indeed, the latter acts as a low-pass filter and by increasing the sample-to-detector distance one achieves stronger suppression of high spatial frequencies in reconstructed projection images and hence stronger reduction of the standard deviation of noise in individual projections as well as in CT reconstructed slices (Nesterets & Gureyev, 2014). It should be emphasized that this reduction of the standard deviation of noise comes with increase of the spatial correlation length of noise in reconstructed images, *i.e.* the system resolution degrades (Gureyev *et al.*, 2013, 2014b). This is clearly observed in Table 9 by analysing the columns containing the values of the spatial resolution (Res). Note, however, that the relative degradation

Table 10

Quality characteristics of CT slices reconstructed (using FBP) from phase-retrieved (using TIE-HOM with $\gamma = 1000$) low-photon-statistics (361 projections) data at the sample-to-detector distance $R_2 = 5$ m, for different X-ray energies.

The values in bold indicate the best result for each quality characteristic.

Index	Material	$E = 38$ keV			$E = 45$ keV			$E = 50$ keV		
		SNR / $D^{1/2}$ (mGy $^{-1/2}$)	Res (μ m)	$Q_s \dagger \times 10^4$ (μ m $^{-1}$ mGy $^{-1/2}$)	SNR / $D^{1/2}$ (mGy $^{-1/2}$)	Res (μ m)	$Q_s \times 10^4$ (μ m $^{-1}$ mGy $^{-1/2}$)	SNR / $D^{1/2}$ (mGy $^{-1/2}$)	Res (μ m)	$Q_s \times 10^4$ (μ m $^{-1}$ mGy $^{-1/2}$)
0	Polycarbonate	6.98 \pm 0.06 [8.03 \pm 0.07]	173.5 [176.5]	402 \pm 3 [455 \pm 4]	7.31 \pm 0.06 [8.57 \pm 0.06]	173.2 [175.3]	422 \pm 3 [489 \pm 4]	7.09 \pm 0.05 [8.10 \pm 0.06]	171.6 [174.0]	413 \pm 3 [465 \pm 3]
1	Glycerol	10.01 \pm 0.09	173.9	576 \pm 5	9.59 \pm 0.07	175.8	546 \pm 4	8.64 \pm 0.06	175.1	494 \pm 4
2	CaCl ₂ 1 M	11.4 \pm 0.1	175.6	651 \pm 6	10.74 \pm 0.08	174.6	616 \pm 5	9.40 \pm 0.07	176.6	533 \pm 4
3	Ethanol 35v%	6.73 \pm 0.06	174.8	385 \pm 3	6.76 \pm 0.05	173.7	389 \pm 3	6.39 \pm 0.05	173.4	369 \pm 3
4	Paraffin oil	6.64 \pm 0.06	177.5	374 \pm 3	7.30 \pm 0.06	174.2	421 \pm 3	6.86 \pm 0.05	174.5	394 \pm 3
5	Water	8.18 \pm 0.07	174.2	469 \pm 4	8.09 \pm 0.06	175.5	461 \pm 3	7.66 \pm 0.05	173.6	442 \pm 3
6	Fatty ham	5.55 \pm 0.05	176.0	316 \pm 3	7.31 \pm 0.06	166.1	440 \pm 3	6.84 \pm 0.05	170.5	401 \pm 3
7	Meaty ham	7.90 \pm 0.07	170.9	463 \pm 4	9.13 \pm 0.07	166.1	549 \pm 4	8.14 \pm 0.06	168.4	484 \pm 3
8	Fibrous ham	8.83 \pm 0.07	167.3	528 \pm 4	9.10 \pm 0.07	169.8	536 \pm 4	8.46 \pm 0.06	168.8	501 \pm 4

$\dagger Q_s = \text{SNR} / D^{1/2} / \text{Res}$.

of the resolution (with respect to the values corresponding to the shortest sample-to-detector distance of 0.27 m) is small (about 25%, for the longest sample-to-detector distance of 5 m); phase retrieval is only one of several factors affecting the spatial resolution in a CT reconstructed volume. This explains, to some extent, the observed increase of the quality index with increasing sample-to-detector distance.

Although not presented in this paper, a behaviour similar to that of the SNR per unit dose was also observed for the CNR per unit dose. Namely, with increasing sample-to-detector distance the CNR per unit dose increased, due to the above-mentioned effect of the TIE-HOM phase-retrieval algorithm. This is because the area contrast in CT reconstructed slices is independent of the sample-to-detector distance, while the standard deviation of noise (after TIE-HOM retrieval) decreases with increasing sample-to-detector distance and, according to equation (4), the CNR increases. Also, we observed an improvement of the FOM (the ratio of the CNR per unit dose to the FWHM of the material boundaries) for the selected materials (glycerol, calcium chloride and paraffin oil) with increasing sample-to-detector distance. This is explained by the observed behaviour of the FWHM of the boundaries between the selected materials and polycarbonate (see Table 7 for details). In particular, Table 7 indicates that in the case of glycerol and paraffin oil the width of the boundaries in CT slices reconstructed using phase-retrieved projections (the values in the parentheses) is usually smaller than in the CT slices reconstructed from contact projections (*i.e.* the projections collected at the sample-to-detector distance of 0.27 m). In the case of calcium chloride, although the width of its boundaries with polycarbonate slightly increases with increasing sample-to-detector distance, by at most 25% with respect to the boundary width in CT slices reconstructed from contact projections, the FOM is still significantly increasing with increasing sample-to-detector distance (for the distances used in this experiment). Since the longest sample-to-detector distance of 5 m resulted in the best quality of CT reconstructed slices (in terms of the quality measures utilized in the paper), in our subsequent analysis we

restrict our consideration to the case of a sample-to-detector distance of 5 m.

We also investigated the dependence of the CT reconstruction quality on the X-ray energy, by comparing values of the above-defined quality measures for CT slices reconstructed using data collected at three X-ray energies: 38 keV, 45 keV and 50 keV.

Analysis of data in Table 10 shows that, for the three X-ray energies used in the experiment, the SNR per unit dose as well as the quality index are monotonically decreasing for glycerol, calcium chloride and water with increasing X-ray energy. For other materials, both quality measures are maximal at the X-ray energy of 45 keV. It is worth mentioning that the observed excellent correlation between the SNR per unit dose and the quality index [which is the ratio of the SNR per unit dose to the system resolution defined above, before equation (4)] can be explained by the fact that the measured system resolution is observed to be independent of the X-ray energy.

Regarding the quality of CT reconstructed slices in terms of the FOM, this can be improved (with respect to CT slices reconstructed from contact projections) using two alternative approaches: (i) by using raw (*i.e.* without phase retrieval) projections collected at a finite sample-to-detector distance, or (ii) by applying TIE-HOM phase retrieval to projection data. In the former case, the CNR is essentially independent of the sample-to-detector distance and the gain in the FOM (with respect to the CT slices reconstructed from contact projections) is totally due to improvement of the boundary sharpness as a result of in-line phase contrast (see Table 11). In the latter case, the CNR is significantly improved as a result of low-pass filtering of projections by the TIE-HOM algorithm (see also discussion above) while the sharpness of the boundaries, compared with the case of CT slices reconstructed from contact projections, is essentially preserved or degraded insignificantly (see Table 12). Comparison of data contained in Tables 11 and 12 allowed us to conclude that, in terms of the FOM and for the chosen value of the parameter γ in the TIE-HOM algorithm, the second approach is advantageous and

Table 11

Quality characteristics of CT slices reconstructed (using FBP) from raw (without phase retrieval) low-photon-statistics (361 projections) data at the sample-to-detector distance $R_2 = 5$ m, for different X-ray energies.

The values in bold indicate the best result for each quality characteristic.

Material combination	$E = 38$ keV			$E = 45$ keV			$E = 50$ keV		
	CNR / $D^{1/2}$ (mGy $^{-1/2}$)	FWHM (μ m)	FOM $\dagger \times 10^4$ (μ m $^{-1}$ mGy $^{-1/2}$)	CNR / $D^{1/2}$ (mGy $^{-1/2}$)	FWHM (μ m)	FOM $\times 10^4$ (μ m $^{-1}$ mGy $^{-1/2}$)	CNR / $D^{1/2}$ (mGy $^{-1/2}$)	FWHM (μ m)	FOM $\times 10^4$ (μ m $^{-1}$ mGy $^{-1/2}$)
Glycerol/polycarb.	0.311 \pm 0.003	242 \pm 16	12.8 \pm 0.8	0.312 \pm 0.002	138 \pm 22	23 \pm 4	0.286 \pm 0.002	207 \pm 34	14 \pm 2
CaCl ₂ /polycarb.	1.059 \pm 0.009	492 \pm 7	21.6 \pm 0.4	0.797 \pm 0.006	385 \pm 17	20.7 \pm 0.9	0.593 \pm 0.004	442 \pm 27	13.5 \pm 0.8
Ethanol/polycarb.	0.0646 \pm 0.0005	–	–	0.1531 \pm 0.0012	–	–	0.1933 \pm 0.0014	–	–
Paraffin/polycarb.	0.583 \pm 0.005	185 \pm 8	31.5 \pm 1.4	0.651 \pm 0.005	138 \pm 13	47 \pm 4	0.624 \pm 0.004	168 \pm 14	37 \pm 3
Water/polycarb.	0.0057 \pm 0.0005	–	–	0.0943 \pm 0.0007	–	–	0.1173 \pm 0.0008	–	–
Polycarb./air	2.35 \pm 0.02	–	–	2.62 \pm 0.02	–	–	2.62 \pm 0.02	–	–
Fatty/meaty ham	0.589 \pm 0.005	–	–	0.573 \pm 0.004	–	–	0.522 \pm 0.004	–	–

\dagger FOM = CNR / $D^{1/2}$ / FWHM.

Table 12

Quality characteristics of CT slices reconstructed (using FBP) from phase-retrieved (using TIE-HOM with $\gamma = 1000$) low-photon-statistics (361 projections) data at sample-to-detector distance $R_2 = 5$ m, for different X-ray energies.

The values in bold indicate the best result for each quality characteristic.

Material combination	$E = 38$ keV			$E = 45$ keV			$E = 50$ keV		
	CNR / $D^{1/2}$ (mGy $^{-1/2}$)	FWHM (μ m)	FOM $\dagger \times 10^4$ (μ m $^{-1}$ mGy $^{-1/2}$)	CNR / $D^{1/2}$ (mGy $^{-1/2}$)	FWHM (μ m)	FOM $\dagger \times 10^4$ (μ m $^{-1}$ mGy $^{-1/2}$)	CNR / $D^{1/2}$ (mGy $^{-1/2}$)	FWHM (μ m)	FOM $\dagger \times 10^4$ (μ m $^{-1}$ mGy $^{-1/2}$)
Glycerol/polycarb.	1.357 \pm 0.012	414 \pm 9	32.7 \pm 0.8	1.120 \pm 0.008	279 \pm 16	40 \pm 2	0.965 \pm 0.007	481 \pm 25	21 \pm 1
CaCl ₂ /polycarb.	4.24 \pm 0.04	626 \pm 3	67.7 \pm 0.7	2.92 \pm 0.02	559 \pm 10	52 \pm 1	2.011 \pm 0.014	528 \pm 12	38.1 \pm 0.9
Ethanol/polycarb.	0.262 \pm 0.002	–	–	0.538 \pm 0.004	–	–	0.664 \pm 0.005	–	–
Paraffin/polycarb.	2.45 \pm 0.02	355 \pm 4	69.1 \pm 0.9	2.37 \pm 0.02	338 \pm 7	70 \pm 2	2.10 \pm 0.02	363 \pm 10	58 \pm 2
Water/polycarb.	0.0170 \pm 0.0002	–	–	0.318 \pm 0.002	–	–	0.437 \pm 0.003	–	–
Polycarb./air	9.66 \pm 0.08	260 \pm 2	372 \pm 4	9.45 \pm 0.07	261 \pm 4	363 \pm 6	8.83 \pm 0.06	251 \pm 4	352 \pm 6
Fatty ham/meaty ham	2.42 \pm 0.02	–	–	2.17 \pm 0.02	–	–	1.69 \pm 0.01	–	–

\dagger FOM = CNR / $D^{1/2}$ / FWHM.

results in up to two- to three-fold improvement of the FOM compared with the first approach.

Also, for three selected materials, including glycerol, calcium chloride and paraffin oil (for which the CNR is relatively large), and for both approaches described above, the optimal X-ray energy that maximizes the FOM is 45 keV, in most cases. This behaviour correlates well with the general trend observed for the energy dependence of the quality index Q_s .

It is worth mentioning that analysis of Table 11 indicates that none of the material pairs (except for polycarbonate and air) can be reliably differentiated when using a threshold of 5 for the CNR (Rose, 1948) and a reasonable MGD of 4 mGy (in order to obtain the CNR for this dose, one needs to multiply the values of CNR/ $D^{1/2}$ by two). On the other hand, analysis of Table 12 shows that TIE-HOM phase retrieval of projections prior to the FBP CT reconstruction results in significant, three- to four-fold, improvement of the CNR. In this case, two materials, calcium chloride and paraffin, can be reliably separated from polycarbonate, at least for the lowest of the three X-ray energies used.

Importantly, analysis of data in Tables 11 and 12 indicates that, in general, the energy dependence of the CNR per unit dose is not uniform. For the X-ray energies used in our

experiment, one can easily reveal three typical behaviours: CNR is (i) decreasing with increasing X-ray energy, which is observed, for example, for glycerol and calcium chloride in polycarbonate and for the pair fatty ham/meaty ham, (ii) increasing with increasing X-ray energy, which is observed for ethanol and water in polycarbonate, and (iii) maximum at the 45 keV energy, which is observed in CT slices reconstructed from raw projections for paraffin oil in polycarbonate. This observation indicates that the optimum X-ray energy that maximizes the CNR per unit dose and the FOM, in general, depends on the choice of the pair of materials. For mammographic application of CT, we expect that fatty ham and meaty ham better represent real breast tissue, compared with other materials in the phantom. As already discussed above, for this pair of tissues, and amongst the three X-ray energies used, the CNR is maximal at 38 keV while the SNR as well as the quality index are maximal at 45 keV.

3.5. Comparison of different CT reconstruction algorithms

We investigated the possibility of improving the quality of CT reconstructions by utilizing four iterative CT reconstruction algorithms, including equal-slope tomography (EST) (Miao *et al.*, 2005; X-TRACT, 2015), iterative FBP (Myers *et*

Table 13

Quality characteristics of CT slices reconstructed (using alternative CT reconstruction algorithms) from phase-retrieved (using TIE-HOM with $\gamma = 1000$) low-photon-statistics (361 projections, except for EST which used 340 projections) data at sample-to-detector distance $R_2 = 5$ m and X-ray energy $E = 38$ keV.

EST (five iterations of gradient algorithm). iFBP (nBins = 512, NSR = 0.004, HistPower-1 = 0, Filter size = 3 pixels, beta threshold = 0). TV (regularization parameter $\beta = 1$, NSR = 0.004, 10 iterations). RL (NSR = 0.004, 200 iterations). The values in bold indicate the best result for each quality characteristic.

Index	Material	EST			iFBP		
		SNR / $D^{1/2}$ (mGy $^{-1/2}$)	Res (μ m)	$Q_S \dagger \times 10^4$ (μ m $^{-1}$ mGy $^{-1/2}$)	SNR / $D^{1/2}$ (mGy $^{-1/2}$)	Res (μ m)	$Q_S \times 10^4$ (μ m $^{-1}$ mGy $^{-1/2}$)
0	Polycarb.	8.81 \pm 0.07	192.3	458 \pm 4	9.26 \pm 0.08	181.4	510 \pm 4
1	Glycerol	13.17 \pm 0.11	194.2	678 \pm 6	11.3 \pm 0.1	182.0	618 \pm 5
2	CaCl ₂ 1 M	16.48 \pm 0.14	193.0	854 \pm 7	15.09 \pm 0.13	181.8	830 \pm 7
3	Ethanol 35v%	9.41 \pm 0.08	194.1	485 \pm 4	8.75 \pm 0.07	183.9	476 \pm 4
4	Paraffin oil	8.98 \pm 0.08	203.7	440 \pm 4	8.01 \pm 0.07	181.7	441 \pm 4
5	Water	10.50 \pm 0.09	196.1	536 \pm 5	9.75 \pm 0.08	183.0	533 \pm 5
6	Fatty ham	7.79 \pm 0.07	161.0	483 \pm 4	8.53 \pm 0.07	160.6	532 \pm 5
7	Meaty ham	11.3 \pm 0.1	189.3	594 \pm 5	9.63 \pm 0.08	176.1	547 \pm 5
8	Fibrous ham	12.67 \pm 0.11	181.9	697 \pm 6	10.57 \pm 0.09	173.2	611 \pm 5

Index	Material	TV			RL		
		SNR / $D^{1/2}$ (mGy $^{-1/2}$)	Res (μ m)	$Q_S \times 10^4$ (μ m $^{-1}$ mGy $^{-1/2}$)	SNR / $D^{1/2}$ (mGy $^{-1/2}$)	Res (μ m)	$Q_S \times 10^4$ (μ m $^{-1}$ mGy $^{-1/2}$)
0	Polycarb.	14.94 \pm 0.13	165.6	902 \pm 8	15.51 \pm 0.13	192.8	805 \pm 7
1	Glycerol	17.43 \pm 0.15	165.2	1055 \pm 9	16.74 \pm 0.14	190.8	878 \pm 7
2	CaCl ₂ 1 M	21.9 \pm 0.2	163.9	1334 \pm 11	15.56 \pm 0.13	186.3	835 \pm 7
3	Ethanol 35v%	14.31 \pm 0.12	166.7	858 \pm 7	17.12 \pm 0.15	190.6	898 \pm 8
4	Paraffin oil	11.9 \pm 0.1	159.6	748 \pm 6	14.03 \pm 0.12	228.8	614 \pm 5
5	Water	15.14 \pm 0.13	166.0	912 \pm 8	16.87 \pm 0.14	192.1	879 \pm 7
6	Fatty ham	13.30 \pm 0.11	154.2	863 \pm 7	13.61 \pm 0.12	162.9	835 \pm 7
7	Meaty ham	15.73 \pm 0.13	165.5	951 \pm 8	17.39 \pm 0.15	181.7	958 \pm 8
8	Fibrous ham	16.44 \pm 0.14	159.2	1033 \pm 9	15.31 \pm 0.13	179.6	853 \pm 7

$\dagger Q_S = \text{SNR} / D^{1/2} / \text{Res}$.

al., 2010; X-TRACT, 2015), an implementation of the total variation (TV) based algorithm (X-TRACT, 2015) and an implementation of the generic Richardson–Lucy (RL) reconstruction algorithm (Richardson, 1972; Lucy, 1974; X-TRACT, 2015). These algorithms have been applied to a single low-photon-statistics projection data set, consisting of 340 projections (with MGD of about 10.2 mGy) in the case of EST and 361 projections (with MGD of about 10.8 mGy) for other algorithms. The data set corresponds to an X-ray energy of 38 keV and the longest sample-to-detector distance of 5 m. TIE-HOM phase retrieval with the parameter $\gamma = 1000$ has been applied to individual projections prior to CT reconstructions.

Reconstructed slices, together with their magnified fragments, are shown in Fig. 8. SNR per unit dose, the spatial resolution and the quality index Q_S are provided in Table 13. CNR per unit dose, edge sharpness and FOM (where available) are given in Table 14. Below we provide brief comparisons, in terms of the quality measures used throughout the paper, of each of the reconstruction algorithms with the conventional FBP algorithm.

EST. Compared with the conventional FBP reconstruction algorithm, this method results in noticeable improvement of most quality measures, including the SNR, the quality index Q_S and the FOM. It also seems to preserve the sharpness of the boundaries but noticeably degrades the spatial resolution. Visually, the reconstructed slices look slightly less noisy.

iFBP. Compared with the conventional FBP reconstruction algorithm, this method performs better in all respects: it improves the SNR and the quality index while only slightly degrading the spatial resolution; it also improves the CNR and the FOM and definitely outperforms the conventional FBP in terms of the boundary sharpness. Compared with EST, iFBP is generally better in terms of boundary sharpness, FOM and spatial resolution but is worse in terms of noise suppression and, as a result, is generally poorer in terms of the SNR and the quality index.

TV. Compared with the conventional FBP reconstruction algorithm, this method shows significant improvements in all respects. Moreover, this method is advantageous in terms of the quality index and the FOM; these are consistently maximal amongst the considered methods. At the same time, this method preserves and even improves the sharpness of boundaries. However, visual inspection of Fig. 8 indicates that this method results in a blocky structure of noise, despite the finest resolution as seen in Table 13.

RL. This method outperforms the conventional FBP reconstruction algorithm in terms of noise suppression, but at the expense of spatial resolution and edge sharpness. It performs significantly better in terms of SNR, quality index and CNR but only slightly better in terms of FOM. Compared with other considered algorithms, this method is undoubtedly the best in terms of the SNR per unit dose and CNR per unit dose (see Tables 13 and 14). However, on account of system

Table 14

Quality characteristics of CT slices reconstructed (using alternative CT reconstruction algorithms) from phase-retrieved (using TIE-HOM with $\gamma = 1000$) low-photon-statistics (361 projections except for EST which used 340 projections) data at the sample-to-detector distance $R_2 = 5$ m and X-ray energy $E = 38$ keV.

The values in bold indicate the best result for each quality characteristic.

Material combination	EST			iFBP		
	CNR / $D^{1/2}$ (mGy $^{-1/2}$)	FWHM (μ m)	FOM $\dagger \times 10^4$ (μ m $^{-1}$ mGy $^{-1/2}$)	CNR / $D^{1/2}$ (mGy $^{-1/2}$)	FWHM (μ m)	FOM $\times 10^4$ (μ m $^{-1}$ mGy $^{-1/2}$)
Glycerol/polycarb.	1.77 \pm 0.02	383 \pm 60	46 \pm 7	1.523 \pm 0.013	238 \pm 85	64 \pm 22
CaCl ₂ /polycarb.	5.96 \pm 0.05	553 \pm 17	108 \pm 3	5.51 \pm 0.05	557 \pm 20	99 \pm 4
Ethanol/polycarb.	0.452 \pm 0.004	–	–	0.401 \pm 0.003	–	–
Paraffin/polycarb.	3.27 \pm 0.03	378 \pm 24	86 \pm 5	2.85 \pm 0.02	226 \pm 20	126 \pm 11
Water/polycarb.	0.0598 \pm 0.00005	–	–	0.0916 \pm 0.0008	–	–
Polycarb./air	15.23 \pm 0.13	387 \pm 5	393 \pm 6	12.98 \pm 0.11	248 \pm 7	523 \pm 15
Fatty/meaty ham	3.13 \pm 0.03	–	–	2.93 \pm 0.02	–	–

Material combination	TV			RL		
	CNR / $D^{1/2}$ (mGy $^{-1/2}$)	FWHM (μ m)	FOM $\times 10^4$ (μ m $^{-1}$ mGy $^{-1/2}$)	CNR / $D^{1/2}$ (mGy $^{-1/2}$)	FWHM (μ m)	FOM $\times 10^4$ (μ m $^{-1}$ mGy $^{-1/2}$)
Glycerol/polycarb.	2.43 \pm 0.02	285 \pm 54	85 \pm 16	2.49 \pm 0.02	935 \pm 51	27 \pm 1
CaCl ₂ /polycarb.	8.35 \pm 0.07	624 \pm 20	133 \pm 4	7.52 \pm 0.06	808 \pm 25	93 \pm 3
Ethanol/polycarb.	0.678 \pm 0.006	–	–	0.717 \pm 0.006	–	–
Paraffin/polycarb.	4.27 \pm 0.04	232 \pm 14	184 \pm 11	5.17 \pm 0.04	613 \pm 18	84 \pm 3
Water/polycarb.	0.151 \pm 0.001	–	–	0.160 \pm 0.002	–	–
Polycarb./air	20.4 \pm 0.2	203 \pm 4	1006 \pm 22	24.1 \pm 0.2	624 \pm 8	387 \pm 6
Fatty/meaty ham	4.76 \pm 0.04	–	–	5.23 \pm 0.04	–	–

\dagger FOM = CNR / $D^{1/2}$ / FWHM.

spatial resolution and boundary sharpness, as quantified by the quality index Q_S and the FOM, the TV-based CT reconstruction algorithm is advantageous while the RL algorithm is the second best, in terms of the quality index (which does not take into account the boundary sharpness) and is the worst in

terms of the FOM which incorporates the boundary sharpness. In fact, this method was found to be the worst in terms of the degradation of the boundary sharpness.

The four iterative CT reconstruction algorithms compared in this section were used with the parameters provided in the

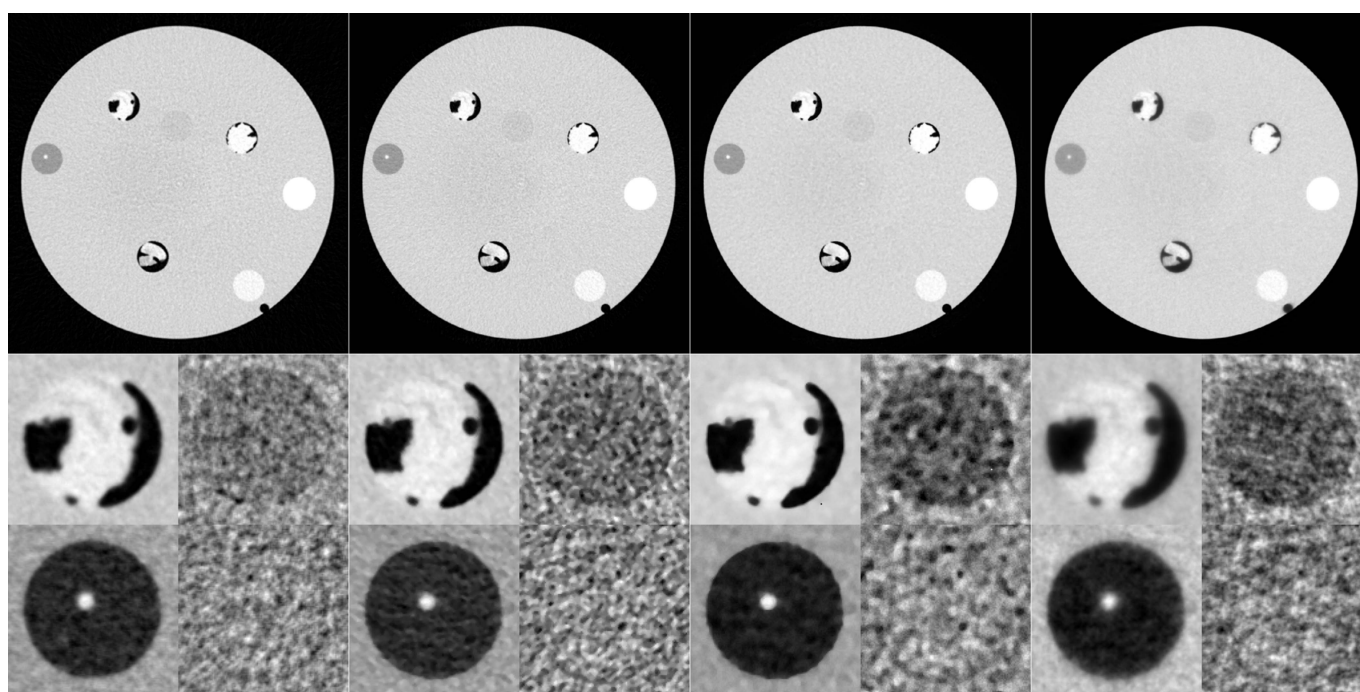


Figure 8

CT slice and its enlarged fragments reconstructed, using four iterative algorithms, from low-photon-statistics (340 projections over 180°, for EST, 361 projections for the rest) phase-retrieved (TIE-HOM with $\gamma = 1000$) projection data set ($E = 38$ keV, $R_2 = 5$ m). From left to right: EST reconstruction, iFBP, TV and RL.

headnote to Table 13. For the EST algorithm, we followed the recommendation provided by the authors of the algorithm to use a few iterations of the gradient algorithm (we used five iterations). The iterative FBP algorithm was found to be sensitive to the noise-to-signal ratio (NSR) parameter. This value was estimated using the object-free fragments of the experimental sinograms. The same NSR value was also used in the TV and RL algorithms. In the case of the TV-based algorithm, we found that its convergence was typically observed after 10–20 iterations and the performance of the algorithm was strongly affected by the regularization parameter β which set the relative weight of the total variation to the goodness-of-fit term in the cost function. With larger values of β , one obtains CT slices with less noise but more smeared details of the object. In the case of the RL algorithm, the number of iterations plays the role of a regularization parameter: by increasing the number of iterations one achieves a better match between the original and calculated sinograms, thus improving the resolution in the reconstructed slices, but amplifying noise. The regularization parameters in the TV and RL algorithms were chosen by visual inspection of the reconstructed slices and thus are very subjective. A more rigorous regularization approach for these two algorithms could be based on finding such regularization parameters that maximize the quality index Q_S or the FOM. This tuning procedure has not been implemented in this paper and will be the subject of our future research.

4. Conclusions

The main outcome of this study is the demonstration of the possibility of producing high-quality X-ray in-line phase-contrast CT images with a conventional flat-panel detector having relatively large (~ 100 mm) pixels. A key feature of this method is the use of long (up to 5 m, in this study) distances between the sample and the detector, which does not induce penumbral blurring of the image as long as the incident X-ray beam has sufficiently high spatial coherence, as available at synchrotron beamlines and with microfocus laboratory X-ray sources. At the same time, the long effective propagation distances can lead to sufficient ‘amplification’ of in-line phase contrast to the extent that it becomes possible to detect and utilize it in spite of the relatively low spatial resolution (broad point-spread function) of the imaging system. Importantly, detectors with large pixels can typically afford a thicker and hence more efficient X-ray scintillator layer, thus resulting in higher quantum efficiency. This in turn allows one to solve the two critical issues which so far have prevented practical applications of in-line phase-contrast CT imaging for medical diagnostic purposes, namely that of long exposure times and large radiation doses (which were primarily due to the use of high-resolution detectors). In this work, we have analysed the effects of key imaging setup parameters, such as the X-ray energy, the sample-to-detector distance, the photon fluence (X-ray dose), as well as image processing steps, including the phase retrieval and advanced CT reconstruction algorithms, on the objective quality characteristics of the resultant images.

We have demonstrated that an optimal combination of the above factors can allow one to produce high-quality in-line phase-contrast CT images of soft-tissue samples at radiologically acceptable doses.

Acknowledgements

We are grateful to Dr Nicola Sodini of Elettra-Sincrotrone Trieste for manufacturing the plastic phantom used in this study. We are also grateful to Ms Clare Scott and Dr Anton Maksimenko of the Australian Synchrotron for the assistance in preparation of the samples and for help in conducting the experiment, respectively. We are also grateful to Dr Jessica Lye of ARPANSA/RMIT for calculating the electron-loss correction factors for an ion chamber used in the experiment. KMP acknowledges financial support from the University of New England. MJK acknowledges funding from the Australian Research Council (ARC) and is an ARC Australian Research Fellow (DP110101941). This research was undertaken on the Imaging and Medical beamline at the Australian Synchrotron, Victoria, Australia.

References

- Beltran, M. A., Paganin, D. M., Siu, K. K., Fouras, A., Hooper, S. B., Reser, D. H. & Kitchen, M. J. (2011). *Phys. Med. Biol.* **56**, 7353–7369.
- Bravin, A., Coan, P. & Suortti, P. (2013). *Phys. Med. Biol.* **58**, R1–R35.
- Ciatto, S., Houssami, N., Bernardi, D., Caumo, F., Pellegrini, M., Brunelli, S., Tuttobene, P., Bricolo, P., Fantò, C., Valentini, M., Montemezzi, S. & Macaskill, P. (2013). *Lancet Oncol.* **14**, 583–589.
- Dance, D. R. (1990). *Phys. Med. Biol.* **35**, 1211–1220.
- Diemoz, P. C., Bravin, A., Langer, M. & Coan, P. (2012). *Opt. Express*, **20**, 27670–27690.
- Gureyev, T. E., Mayo, S. C., Nesterets, Y. I., Mohammadi, S., Lockie, D., Menk, R. H., Arfelli, F., Pavlov, K. M., Kitchen, M. J., Zanconati, F., Dullin, C. & Tromba, G. (2014a). *J. Phys. D*, **47**, 365401.
- Gureyev, T., Mohammadi, S., Nesterets, Y., Dullin, C. & Tromba, G. (2013). *J. Appl. Phys.* **114**, 144906.
- Gureyev, T. E., Nesterets, Y. I., de Hoog, F., Schmalz, G., Mayo, S. C., Mohammadi, S. & Tromba, G. (2014b). *Opt. Express*, **22**, 9087–9094.
- Gureyev, T. E., Nesterets, Y., Ternovski, D., Thompson, D., Wilkins, S. W., Stevenson, A. W., Sakellariou, A. & Taylor, J. A. (2011). *Proc. SPIE*, **8141**, 1–14.
- Gureyev, T. E., Stevenson, A. W., Nesterets, Y. I. & Wilkins, S. W. (2004). *Opt. Commun.* **240**, 81–88.
- Hammerstein, R. G., Miller, D. W., White, D. R., Masterson, E. M., Woodard, H. Q. & Laughlin, J. S. (1979). *Radiology*, **130**, 485–491.
- Johns, P. C. & Yaffe, M. J. (1985). *Med. Phys.* **12**, 289–296.
- Lucy, L. B. (1974). *Astron. J.* **79**, 745–754.
- Malliori, A., Bliznakova, K., Speller, R. D., Horrocks, J. A., Rigon, L., Tromba, G. & Pallikarakis, N. (2012). *Med. Phys.* **39**, 5621–5634.
- Miao, J., Förster, F. & Levi, O. (2005). *Phys. Rev. B*, **72**, 052103.
- Myers, G. R., Thomas, C. D. L., Paganin, D. M., Gureyev, T. E. & Clement, J. G. (2010). *Appl. Phys. Lett.* **96**, 021105.
- NCRP (2004). *A Guide to Mammography and Other Breast Imaging Procedures*. NCRP Report No. 149. Bethesda, MD: National Council on Radiation Protection and Measurements.
- Nesterets, Y. I. & Gureyev, T. E. (2009). *Proceedings of the 18th World IMACS Congress and MODSIM09 International Congress on Modelling and Simulation*, edited by R. S. Anderssen, R. D. Braddock & L. T. H. Newham, pp. 1045–1051.
- Nesterets, Y. I. & Gureyev, T. E. (2014). *J. Phys. D*, **47**, 105402.

- Olivo, A., Gkoumas, S., Endrizzi, M., Hagen, C. K., Szafraniec, M. B., Diemoz, P. C., Munro, P. R., Ignatyev, K., Johnson, B., Horrocks, J. A., Vinnicombe, S. J., Jones, J. L. & Speller, R. D. (2013). *Med. Phys.* **40**, 090701.
- Pacilè, S., Brun, F., Dullin, C., Nesterets, Y. I., Dreossi, D., Mohammadi, S., Tonutti, M., Stacul, F., Lockie, D., Zanconati, F., Accardo, A., Tromba, G. & Gureyev, T. E. (2015). *Biomed. Opt. Express*, **6**, 3099.
- Paganin, D., Mayo, S. C., Gureyev, T. E., Miller, P. R. & Wilkins, S. W. (2002). *J. Microsc.* **206**, 33–40.
- Pisano, E. D., Gatsonis, C., Hendrick, E., Yaffe, M., Baum, J. K., Acharyya, S., Conant, E. F., Fajardo, L. L., Bassett, L., D'Orsi, C., Jong, R. & Rebner, M. (2005). *N. Engl. J. Med.* **353**, 1773–1783.
- Richardson, W. H. (1972). *J. Opt. Soc. Am.* **62**, 55–59.
- Rose, A. (1948). *J. Opt. Soc. Am.* **38**, 196–208.
- Sijbers, J. & Postnov, A. (2004). *Phys. Med. Biol.* **49**, N247–N253.
- Stevenson, A. W., Mayo, S. C., Häusermann, D., Maksimenko, A., Garrett, R. F., Hall, C. J., Wilkins, S. W., Lewis, R. A. & Myers, D. E. (2010). *J. Synchrotron Rad.* **17**, 75–80.
- Teague, M. R. (1983). *J. Opt. Soc. Am.* **73**, 1434–1441.
- Thompson, D., Nesterets, Y. I., Gureyev, T. E., Sakellariou, A., Khassapov, A. & Taylor, J. A. (2011). *Proceedings of MODSIM2011 – 19th International Congress on Modelling and Simulation*, edited by F. Chan, D. Marinova and R. S. Anderssen, Perth, Australia, 12–16 December 2011, pp. 620–626.
- X-TRACT (2015). *X-TRACT*, <http://www.ts-imaging.net/Services/AppInfo/X-TRACT.aspx>.
- Zhao, Y. Z., Brun, E., Coan, P., Huang, Z. F., Sztrókay, A., Diemoz, P. C., Liebhardt, S., Mittone, A., Gasilov, S., Miao, J. W. & Bravin, A. (2012). *Proc. Natl Acad. Sci. USA*, **109**, 18290–18294.
- Zysk, A. M., Brankov, J. G., Wernick, M. N. & Anastasio, M. A. (2012). *Med. Phys.* **39**, 906–911.